Delay and Dispersion Effects in Dynamic Susceptibility Contrast MRI: Simulations Using Singular Value Decomposition

Fernando Calamante,* David G. Gadian, and Alan Connelly

Dynamic susceptibility contrast (DSC) MRI is now increasingly used for measuring perfusion in many different applications. The quantification of DSC data requires the measurement of the arterial input function (AIF) and the deconvolution of the tissue concentration time curve. One of the most accepted deconvolution methods is the use of singular value decomposition (SVD). Simulations were performed to evaluate the effects on DSC quantification of the presence of delay and dispersion in the estimated AIF. Both delay and dispersion were found to introduce significant underestimation of cerebral blood flow (CBF) and overestimation of mean transit time (MTT). While the error introduced by the delay can be corrected by using the information of the arrival time of the bolus, the correction for the dispersion is less straightforward and requires a model for the vasculature. **Magn Reson Med 44:466–473, 2000.** © 2000 Wiley-Liss, Inc.

Key words: cerebral blood flow; dynamic susceptibility contrast; singular value decomposition; numerical simulation

There are two commonly used approaches to measuring cerebral blood flow (CBF) using MRI (1). One of these, arterial spin labeling (ASL), uses magnetically labeled blood water as an endogenous tracer (2–6), and it has been used primarily in functional brain mapping studies (1). The second, dynamic susceptibility contrast MRI (DSC-MRI), requires the injection of a bolus of an MR paramagnetic contrast agent and the rapid measurement of the MRI signal loss during its passage through the tissue (7,8). This approach has been used in a large number of applications (1), and is the most commonly used MR perfusion technique in clinical studies of cerebral ischemia.

The quantification of DSC-MRI data is based on the indicator dilution theory, and requires the measurement of the arterial input function (AIF) for the deconvolution of the concentration time curve (1), $C(t)$:

$$C(t) = \frac{\rho}{k_H} \cdot F \cdot (C_a(t) \otimes R(t)), \qquad [1]$$

where F is the CBF, $C_a(t)$ is the AIF, $R(t)$ is the residue function (1), ρ is the density of brain tissue, and k_H accounts for the hematocrit difference between capillaries and large vessels (for simplicity, a value of 1 for ρ and k_H

Radiology and Physics Unit, Institute of Child Health, University College London, London, UK.

Great Ormond Street Hospital for Children NHS Trust, London, UK.

is assumed throughout the rest of the study). There are several methods for performing the deconvolution in Eq. [1], and a model-independent approach using singular value decomposition (SVD) has been shown to be one of the most reliable options (9–11). One of the fundamental assumptions in the quantification of DSC-MRI data is the absence of delay and dispersion of the bolus between the site where the AIF is measured and the most distant tissue; that is, the model assumes that the AIF reflects the *exact* input to the tissue. However, the AIF is typically estimated in a major artery such as the middle cerebral artery (MCA), and this single measurement is usually used as the AIF for the whole brain. Therefore, delay and dispersion can be present, and the quantification may be inaccurate. Such delay and dispersion occur primarily in patients with cerebrovascular diseases, but they may also be present in healthy volunteers (12).

This study describes simulations performed to evaluate the effect of delay and dispersion in the quantification of DSC-MRI data using SVD.

METHODS

Simulations

Simulated AIF

Simulations were performed using AIFs with a shape and size that could typically be obtained using a standard bolus injection scheme. This was done by adjusting the parameters of a gamma-variate function (13):

$$C_a(t) = \begin{cases} 0 & t \leq t_0 \\ C_0(t - t_0)^r e^{-(t-t_0)/b} & t > t_0, \end{cases} \qquad [2]$$

to resemble the arterial bolus size and shape observed in large vessels in typical human studies. The parameter t_0, usually called "bolus arrival time" (BAT), determines the time at which the bolus arrives at any given region.

Since the injected dose is usually proportional to body weight, the amount of injected contrast agent is much smaller in children than in adults. Therefore, much narrower peaks are usually observed in DSC studies in children. For these reasons, two different AIFs were used in the simulations: one that reflected typical data in children ($r = 3.26$, $b = 1.02$ sec, representative of typical datasets obtained at the Great Ormond Street Hospital for Children), and the other, data in adults ($r = 3.0$, $b = 1.5$ sec, as reported in Ref. 9).

Simulation of the Noise Contribution

The contribution of noise to the data can be simulated by adding random Gaussian noise to generate different data-sets for a given signal-to-noise ratio (SNR), as in Monte Carlo simulations (9,11,14,15). This procedure is usually repeated many times (typically ~1000 times), and mean values for the desired parameters are calculated. An alternative approach consists of the acquisition of real datasets of noise, which are then added to the simulated data. This second approach was chosen for the simulations described here since it makes no assumption regarding the noise distribution and it can be directly compared to real data. A typical spin-echo echo planar imaging (EPI) sequence (TE/TR = 100/1500 ms) was used to acquire 50 images of 128 × 128 pixels, using a 1.5 T Siemens Vision whole body imaging system. The manufacturer's standard spherical head phantom was used, together with a cylindrical loading ring. This ring is designed to load the coil to a similar level as found in vivo. The slices were positioned outside the phantom, and since amplitude data were used a constant offset was added to the complex data to preserve the negative contribution to the noise distribution. In this way, both the noise distribution within an image and between images in the dataset (i.e., the noise in the time course for each pixel) reflected typical noise found in real DSC-MRI measurements.

Simulated Tissue Signal (C(t))

For the simulation of the tissue dataset, Eq. [1] was used with the simulated AIF and a residue function R(t). This method requires the assumption of a given model for the tissue. A well-known model is the use of an exponential decay as a general model for the residue function. This is based on a simple model of the vasculature bed as one single, well-mixed compartment (16,17):

$$R(t, MTT) = e^{-t/MTT}. \qquad [3]$$

According to Eq. [1], the simulated tissue signal will be given by:

$$C(t) = FC_0 e^{-(t/MTT - t_0/b)} \int_{t_0}^{t} (\tau - t_0)^r e^{-\tau(1/b - 1/MTT)} d\tau. \qquad [4]$$

By making the appropriate change of variables, an analytical expression can be obtained for the above integral, for the case of b<MTT:

$$C(t) = FC_0 e^{-(t - t_0)/MTT} \left(\frac{1}{b} - \frac{1}{MTT} \right)^{-(r+1)} \Gamma(r + 1)$$
$$\cdot \Gamma_I(r + 1, (t - t_0)(1/b - 1/MTT)), \qquad [5]$$

where Γ(x) is the Gamma function:

$$\Gamma(x) = \int_0^\infty \xi^{x-1} e^{-\xi} d\xi, \qquad [6]$$

Table 1
Values of CBF, CBV, and MTT Used in the Simulations of the Tissue Data (1,18–20)

Tissue type	CBF [ml/100 g/min]	CBV [ml/100 g]	MTT [sec]
Gray matter	60	4	4
White matter	25	2	4.8

and Γ_I(a,x) is the incomplete Gamma function:

$$\Gamma_I(a, x) = \frac{\int_0^x \xi^{a-1} e^{-\xi} d\xi}{\Gamma(a)}. \qquad [7]$$

The scaling factor C_0 was determined from the desired peak drop, Δ, in the simulated signal intensity (1):

$$\Delta = \frac{\Delta S}{S_0} = \frac{S_0 - S_{min}}{S_0} = 1 - e^{-\kappa C_{max} TE}, \qquad [8]$$

where S_0 and S_{min} are the baseline and minimum signal intensities, respectively, C_{max} is the maximum concentration, and κ is a proportionality constant ($\kappa = 1$ assumed for the simulations). Typical values for the signal reductions (from the Great Ormond Street Hospital for Children data and Ref. 9) for gray matter ($\Delta_{gm} = 40\%$) and white matter ($\Delta_{wm} = 17\%$) were chosen; Table 1 shows the values used as representative for CBF, CBV, and MTT (MTT = CBV/CBF) for gray and white matter (1,18–20).

The time concentration curves were then converted to the simulated MRI signal intensity time curves by using the single exponential relationship:

$$S(t) = S_0 e^{-\kappa C(t) TE} \qquad [9]$$

where the baseline S_0 was scaled to the real noise data according to typical *SNR* values obtained in vivo at the Great Ormond Street Hospital for Children (SNR$_{gm}$ = 36 and SNR$_{wm}$ = 30):

$$S_0 = SNR \cdot SD_{noise} \qquad [10]$$

and SD_{noise} was determined from the real noise data.

Simulation of Delay and Dispersion

Since it is not practically possible to measure the *true* AIF (C_a) for each pixel, this is usually estimated from a major vessel, such as the MCA. Therefore, as mentioned in the Introduction, the *estimated* AIF ($C_a^{(est)}$) may undergo delay and/or dispersion during its passage from the point of measurement (MCA) to the particular pixel of tissue.

A delay can be easily simulated by increasing the bolus arrival time (t_0 replaced by $t_0 + \delta t_0$), which effectively shifts the concentration time curve. The dispersion can be described in terms of a transport function. Since the transport function gives the probability distribution for each transit time (1), the dispersion can be described mathemat-

ically as a convolution with a vascular transport function $h^*(t)$ from the site of measurement to the given pixel, i.e.:

$$C_a(t) = C_a^{(est)}(t) \otimes h^*(t) \qquad [11]$$

with the resulting tissue concentration expressed as:

$$C(t) = F \cdot C_a(t) \otimes R(t) = F \cdot (C_a^{(est)}(t) \otimes h^*(t)) \otimes R(t)$$
$$= F \cdot C_a^{(est)}(t) \otimes (h^*(t) \otimes R(t)). \qquad [12]$$

Therefore, it is equivalent to a convolution of the estimated AIF with an effective residue function (9): $R^{(eff)} = h^* \otimes R$.

The particular vascular transport function depends on several factors, such as the topology of the vasculature, the tissue type, the site where the AIF was estimated, CBV, etc. As a first approximation, the same assumption as a well-mixed compartment was used also for the vasculature, and the transport function will be given by (1):

$$h^*(t) = -\frac{dR^*(t)}{dt} = \beta \cdot e^{-\beta t} \qquad [13]$$

where R^* is the residue function associated to h^*, and $1/\beta$ corresponds to the effective "MTT" from the site of AIF measurement to the input to the particular pixel (see Eq. [3]). Therefore, the larger the $1/\beta$, the larger the dispersion, and in the limit of $1/\beta \rightarrow 0$, h^* tends toward the Dirac delta function.

With this model, the effective residue function will be:

$$R^{(eff)}(t) = \frac{\beta}{\left(\dfrac{1}{MTT} - \beta\right)} (e^{-\beta t} - e^{-t/MTT}). \qquad [14]$$

The dispersed tissue concentration time curve will be given by the convolution in Eq. [12]. For the case when $b < MTT$ (valid for the parameters chosen in the simulations) and $b < 1/\beta$, the following analytical expression can be obtained:

$$C(t) = \frac{\beta F C_0 \Gamma(r+1)}{\left(\dfrac{1}{MTT} - \beta\right)} \left[\frac{e^{-\beta(t-t_0)}}{\left(\dfrac{1}{b} - \beta\right)^{r+1}} \Gamma_I(r+1,(t-t_0)\right.$$

$$\times (1/b - \beta)) - \frac{e^{-(t-t_0)/MTT}}{\left(\dfrac{1}{b} - \dfrac{1}{MTT}\right)^{r+1}} \Gamma_I(r+1,(t-t_0)$$

$$\left. \times (1/b - 1/MTT)) \right]. \qquad [15]$$

For the case when $b > 1/\beta$, the second term remains the same (because $b < MTT$; see Eq. [5]), but the first term needs to be evaluated by numerically solving the integral.

This dispersed tissue concentration is shown in Fig. 1 for a range of values of $1/\beta$ together with the original nondispersed tissue curve. A clear spread of the peak and
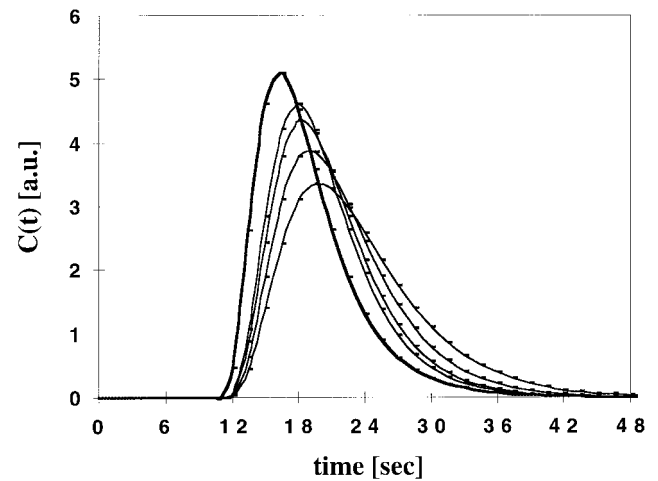

FIG. 1. Effect of dispersion on the tissue concentration for gray matter in the child case. The bold line represents the nondispersed case ($1/\beta = 0$, see Eq. [5]), while the other curves show the concentration for a range of values of $1/\beta$ (progressively, from left to right: 1.5, 2.0, 3.0, and 4.5 sec).

decreasing of its height can be seen with increasing dispersion (increasing $1/\beta$).

Simulation of Image Datasets

For the generation of images, four different time courses were simulated:

1) Time course for a typical gray matter pixel (using Eq. [5]).
2) Time course for a typical white matter pixel (using Eq. [5]).
3) Time course for the delayed and/or dispersed gray matter pixel (using Eq. [15]).
4) Time course for the delayed and/or dispersed white matter pixel (using Eq. [15]).

Each of these time courses was added to one of the four quadrants of the images in the noise dataset (Fig. 2):

- Time course for a typical gray matter pixel: top left side of the image.
- Time course for a typical white matter pixel: bottom left side of the image.
- Time course for the delayed and dispersed gray matter pixel: top right side of the image.
- Time course for the delayed and dispersed white matter pixel: bottom right side of the image.

Before combining the time course of the pixels with the noise data, the positive offset added to the amplitude noise data (see Simulation of the Noise Contribution) was subtracted to bring the noise distribution back around its zero mean.

Therefore, this simulation creates a dataset of 50 images of 128×128 pixels, similar to the one obtained in a typical real DSC-MRI study. Each simulated image consists of four uniform regions (Fig. 2): two "normal" regions (left side of the image) and two "abnormal" regions (right side of the image). By comparing the results from corresponding re-
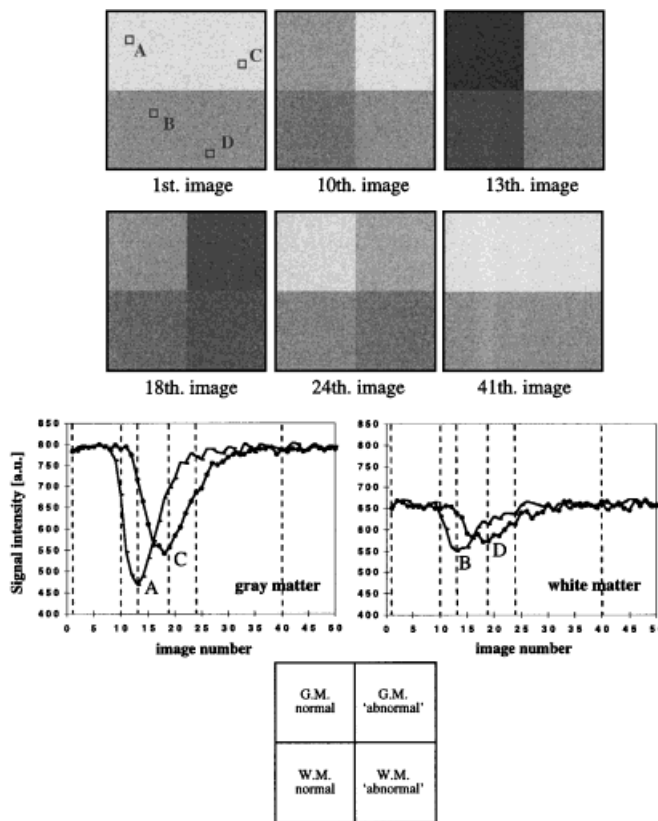
FIG. 2. Simulated images for the case of the adult data with a 3.0-sec delay and $1/\beta = 4.5$ sec. The figure shows six representative images from the set of 50, as well as the time courses from four 3×3 ROIs (as shown by the squares in the first image): region A (gray matter without delay or dispersion), region B (white matter without delay or dispersion), region C (gray matter with 3.0-sec delay and 4.5-sec dispersion), region D (white matter with 3.0-sec delay and 4.5-sec dispersion). The vertical dotted lines in the time course graphs show the positions for the six images displayed.

gions from the images on the left and the right, the effect of different delays and/or dispersions can be evaluated.

A 3×3 uniform smoothing kernel was applied to the simulated raw image data before deconvolution using SVD (9). Maps of CBF, CBV, and MTT were calculated on a pixel-by-pixel basis using software developed by Østergaard et al. (9). The simulations were repeated for a range of delays between 0–6 sec. From our experience, delays between 2–3 sec are not uncommon in patients with cerebrovascular disease, and the 6-sec delay limit was chosen to include all delays that we observed in practice. For the dispersion, data were simulated with values of $1/\beta$ up to 6 sec. This maximum effective "MTT" was taken as an extreme case. A combination of delay and dispersion within these ranges was simulated to evaluate their effect in the quantification of DSC data using SVD. A region of interest in each quadrant of the image was drawn, and the ratios of the "abnormal" to the corresponding normal side were computed for each case. These are shown as mean ± SD over the ~3800 pixels in each region (62×62; the border 2 pixels in each quadrant are not included due to 3×3 kernel used for smoothing). In the absence of delay and dispersion the ratio would be 1, while a ratio < 1

represents an underestimation, and a ratio > 1 represents an overestimation of the corresponding parameters (CBF, CBV, or MTT) due to the presence of delay or dispersion.

RESULTS

Delay Effects (Without Dispersion)

The effect of the simulated delays on the quantification of DSC using SVD can be seen in Fig. 3. This figure shows the ratio of the value in the right region ("abnormal") to the value in the left region ("normal") for the three different parameters (CBF, CBV, and MTT). Figure 3a shows the results for the data using the AIF for children, while Fig. 3b shows the equivalent results for the adult case. The behavior is qualitatively similar for both adult and child cases, regardless of the tissue type. However, the error bars are larger for white matter due to its lower SNR.

As expected, the CBV (which is proportional to the area under the peak) is not affected by the simulated delay, since a delay only shifts the peak, without modifying its shape or size. On the other hand, the CBF is underestimated (ratio < 1) but, interestingly, the flow ratio decreases approximately linearly until a delay of ~1.5–2.0 sec, then oscillates around an asymptotic value of ~0.65, i.e., a 35% underestimation. Correspondingly, the MTT is overestimated, with the ratio increasing very rapidly until delays ~1.5–2.0 sec, and oscillating around an asymptotic value of ~1.6 (i.e., an approximately 60% overestimation).

If there were a significant recirculation peak and a gamma-variate fit to the tissue data were not used to remove its contribution, a fixed time window for the analysis should be used. In this case, the peak would be shifted partly outside the window by the presence of a delay and its effect, in principle, can be much more important. This situation was simulated by fixing the upper limit for the window for the SVD analysis to the time when recirculation typically occurs (~14 sec from the arrival of the bolus in the child case). The results of a fixed time window are shown in Fig. 4 for the data using the AIF for children. The most obvious effect is on the calculated CBV, which is underestimated, since the area within the selected window is less than the total area under the peak. Interestingly, a fixed time window does not seem to modify the results for the CBF calculation, provided the maximum of the peak is within the window (delay ~7.5 sec in Fig. 4). For longer delays, the CBF is further underestimated, because the part of the function inside the window is no longer in the form of a peak. However, such very long delays are unlikely to happen in real data. For the MTT, the initial overestimation is very quickly overcompensated by the fast decrease in CBV, therefore producing an underestimation for delays longer than ~4–5 sec.

As a real example of the effect of delay, Fig. 5 shows the DSC data from a 6-year-old child who had a right internal carotid artery stenosis with probable dissection, and who presented with multiple episodes of transient ischemic attacks. The CBF map (Fig. 5a) shows apparently reduced perfusion in the right hemisphere (left side of the image). Figure 5b shows the concentration time curves for two regions (one in each hemisphere). It can be seen that there
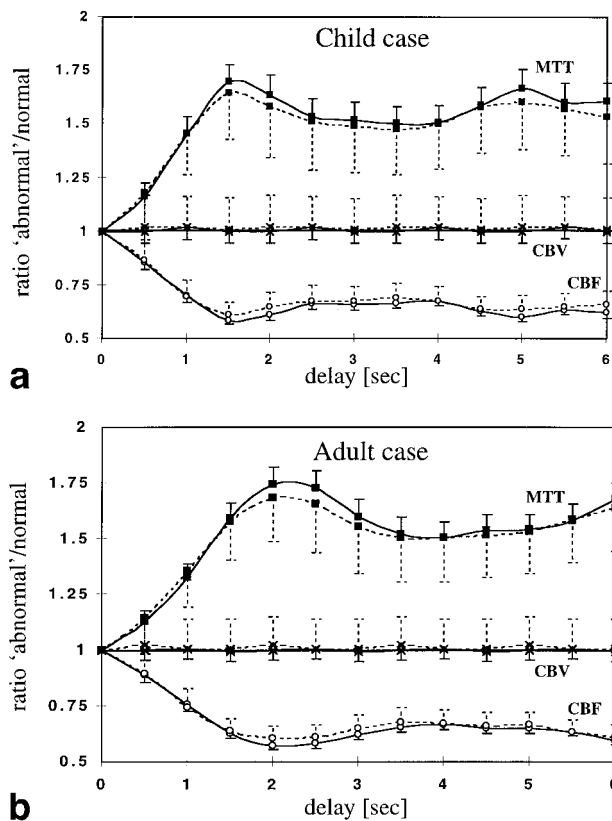
FIG. 3. Effect of delay (without dispersion) on the quantification of DSC-MRI data. The figure shows the ratio of the value in the "abnormal" side to the value in the "normal" side. The solid lines represent the values for gray matter, while the dotted lines show those for white matter. **a:** Child case. **b:** Adult case. CBF ratios are labeled with open circles, CBV ratios with crosses, and MTT ratios with filled squares. The error bars represent the SD of the ratio (21), and only one side of the error bars are displayed to avoid the superposition of the bars from gray and white matter.

is a delay of ~2 sec in the arrival of the bolus to the right side, and although the peak is much wider, its height is similar to that on the left side. Given the simulation data presented in Fig. 3a, we believe that the CBF map shown in Fig. 5a is potentially misleading in that the presence of delay (and possibly dispersion) has introduced an approximately 40% underestimation in the perfusion quantification.

Dispersion Effects (Without Delay)

The effect of the simulated dispersion on the quantification of DSC using SVD can be seen in Fig. 6 (filled squares). This figure shows the ratio of the value in the right region ("abnormal") to the value in the left region ("normal") for the CBF (Fig. 6a) and MTT (Fig. 6b). The left graphs show the results for the data using the AIF for children, while the graphs on the right show the equivalent results for the adult case. As with the delay simulations, the behavior is qualitatively similar for both cases.

Similar to the delayed cases, the CBV is not affected (data not shown): although the shape of the peak changes, the total area under the peak remains the same. The CBF is

increasingly underestimated (ratio < 1) with a larger dispersion and, therefore, the MTT is overestimated. The effect is larger in the gray matter than in the white matter region, especially with increased dispersion.

The maximum CBF underestimation obtained with the simulated delayed data was ~40% (ratio ~0.6), for a delay of approximately 2 sec. An equivalent underestimation is very quickly reached with a dispersion of $1/\beta$ ~1.5–2 sec, but in the case of dispersion, this continues to increase further thereafter as $1/\beta$ increases.

Delay and Dispersion Effects

The combined effect of delay and dispersion on the quantification of DSC using SVD can be seen in Fig. 6. This figure shows the ratios of the value in the right region ("abnormal") to the value in the left region ("normal") as a function of dispersion for different delays. The results for the CBF ratios are shown in Fig. 6a, and the results for the MTT ratios in Fig. 6b. The behavior is qualitatively similar for the child (left graphs) and adult (right graphs), although the errors (underestimation of CBF and overestimation of MTT) are slightly larger for the former. As may be expected, for small dispersion the contribution of the delay is significant, while it becomes less important with increasing dispersion. Furthermore, the ratio is almost independent of the delay value for delays longer than ~1.5–2.0 sec, as was found for the simulated delays without dispersion (see Fig. 3).

DISCUSSION

The effect of various delays and/or dispersions on the SVD analysis of DSC-MRI data have been evaluated using computer simulations. The present study is not intended as a validation of the DSC-MRI technique but to investigate the errors introduced by an unaccounted delay and dispersion. The results are therefore expressed as ratios relative to the value in the absence of delay and dispersion. Although some concern remains regarding the use of DSC-
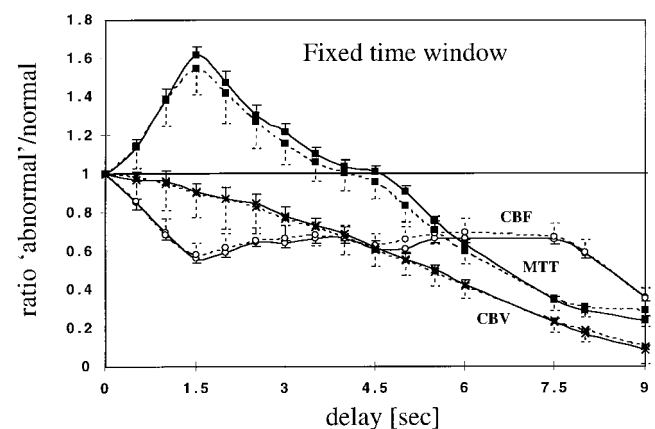

FIG. 4. Effect of delay (without dispersion) on the quantification of DSC-MRI data when a fixed time window is used for the SVD analysis. The figure shows the ratio of the value in the "abnormal" side to the value in the "normal" side for the child case. See legend of Fig. 3 for details.
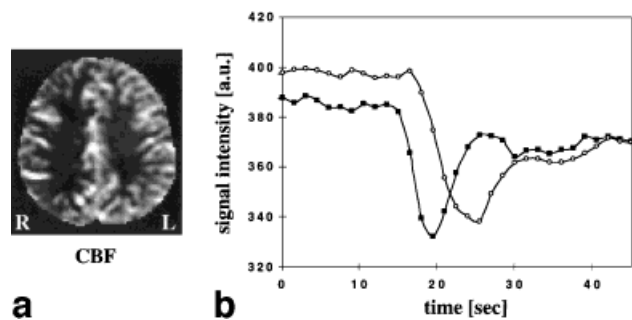
FIG. 5. DSC data from a 6-year-old child who had a right internal carotid artery stenosis with probable dissection. **a:** CBF map. **b:** Signal intensity time curves for two white matter regions (filled squares: left; open circles: right). A clear delay of ~2 sec in the arrival of the bolus can be seen in the right side. The presence of such delay (and possibly dispersion) introduced a significant under-estimation in the CBF map. The measured right to left ratio in the CBF map is 0.55.

MRI for absolute quantification, some studies have reported relative values which agree well with the expected gray-to-white matter ratios in human brain (for review, see Ref. 1).

Two different AIFs were simulated to evaluate the effects of delay and dispersion in both children and adults. By using hand injection for the delivery of the bolus of contrast agent, very different shapes of AIF can be obtained. However, an increasing number of groups are now using MR compatible power injectors. This allows not only a faster injection rate, but also a more reproducible and controlled injection. The simulated AIFs used in this chapter were representative of data from children and adults using a power injector.

The model of vascular transport function assumed for these simulations is one that is commonly used. There are other, simpler models (9,10), such as a box-shaped residue function (representative of a vascular bed with "plug flow"), a triangular function or the decreasing portion of a Gaussian residue function (as intermediate models between the single, well-mixed compartment and the model of parallel capillaries with equal transit times and "plug flow"). Some authors have also suggested the use of linear combination of exponentials (22). More recently, Østergaard et al. (23) incorporated a more complicated mathematical vascular model into the DSC analysis to try to account for the effect of delay and dispersion. In that study, the vasculature was modeled as a major feeding artery (with fixed relative dispersion and a delay determined by its volume fraction) in series with small parallel vessels (considered as simple delay lines) with relative flows and weights according to a given flow heterogeneity. For the simulations described in the present work, the single exponential model was taken as a first approximation for the vascular model. Further studies are needed to verify the validity of the present results with other models, as well as a comparison of the different models. Further work is also necessary to determine the best vascular operators that describe a large range of vascular residue functions.

The simulations used samples of real noise data. This approach was chosen because it has the advantage that no

assumption is made regarding the noise distribution (in contrast to Monte Carlo simulations), and is more directly comparable to real data. Since the measurements were performed in a standard whole-body clinical system using the manufacturer's RF coil, the results should reflect those obtained in many other typical clinical systems. Furthermore, since the results were qualitatively similar for gray and white matter, but with larger error bars in the latter, the results are probably qualitatively true for other SNR as well.

Delay Effects

The presence of a delay in the data was found to introduce large errors in the quantification of CBF and MTT, although it did not affect the CBV (the apparently larger effect in MTT is due to the inverse relationship between CBF and MTT, for a constant CBV).

These errors could be corrected, in principle, by shifting back the peaks by δt_0, although this requires knowledge of the delay for each pixel. An estimation of this delay can be obtained by fitting the concentration time curve to a gam-
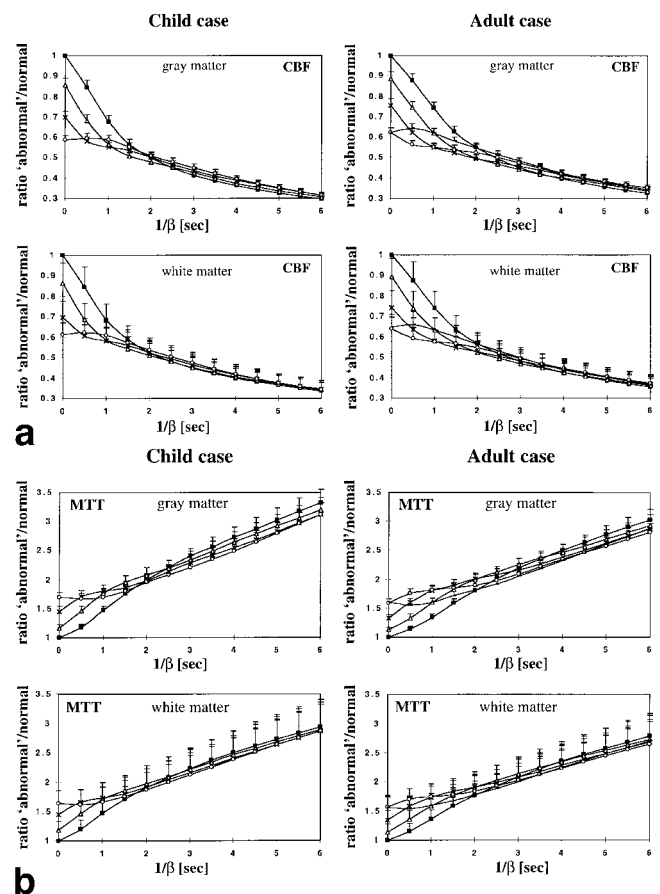

FIG. 6. Effect of delay and dispersion on the quantification of DSC-MRI data. The figure shows the ratio of the value in the "abnormal" side to the value in the "normal" side as a function of dispersion (1/β) for different delays. **a:** CBF. **b:** MTT. The graphs in the top row show the gray matter case, and the graphs in the bottom row the white matter data. The different delays are labeled with different symbols: filled square (0.0 sec), open triangle (0.5 sec), cross (1.0 sec), open circle (1.5 sec), and dash (3.0 sec).

ma-variate function on a pixel-by-pixel basis, although this method is very sensitive to noise.

The qualitative behavior was the same for the two AIFs simulated. However, the delay for which the maximum error was introduced was longer for the adult case (~2–2.5 s) than for the child case (~1.5 s). This most likely reflects the much wider peak for the adult example.

The oscillation about an asymptote of the ratios of CBF and MTT for large delays was an unexpected result. The reasons for this oscillation are not clear. It may depend on the chosen model (exponential), the type of deconvolution (SVD), or the deconvolution process itself, and further work is needed to clarify its origin.

As mentioned in the Results section, a gamma-variate fitting is not performed in many practical cases. The SNR is often not high enough to allow an accurate fitting on a pixel-by-pixel basis, and therefore a fixed time window must be used for the analysis. The simulations showed that the error in the calculated CBF (underestimation) is not greatly affected by the presence of a fixed time window, but that a large error (underestimation) is introduced in the CBV reducing, therefore, the initial overestimation in the MTT.

Dispersion Effects

The simulated dispersions introduced large errors in the quantification of CBF and MTT, while CBV was not affected. In contrast to the effects of delay, the error continued to increase with increasing dispersion, introducing errors over 200% in the MTT and 50% in the CBF for $1/\beta$ larger than ~2.5 sec. This larger error with increasing dispersion can be interpreted in terms of the failure of the DSC model to distinguish between dispersion in the feeding vessels (from the place where the AIF was estimated to the VOI) and intravoxel dispersion by tissue microvasculature within the VOI (1,18,23). An unaccounted dispersion produces spreading of the peak (see Fig. 1), which is interpreted by the DSC model as an increase in the MTT through the tissue (the wider the peak, the longer the MTT). However, this apparent increase in MTT is not related to true intravoxel dispersion.

Unlike the case for a delay, there is no simple way of correcting for dispersion. This requires modeling of the vasculature. As mentioned above, Østergaard et al. (23) recently incorporated a mathematical vascular model into the DSC analysis. By analyzing data from six normal volunteers, they showed that the vascular model approach is less sensitive to vascular delay and dispersion than the conventional SVD approach. This method could potentially be used to correct for the dispersion observed in cerebrovascular disease. Their results are very promising, but further validation on a large number of patients with cerebrovascular diseases is needed. Another possibility would involve the use of the information from the graphs shown in Fig. 6 as a correction. However, this method would also be dependent on the assumed model for the vasculature (a single, well-mixed compartment) and it would require an estimation of β (for example, $1/\beta \sim$ delay). Regardless of the correction method, the simulations performed in this study show that the presence of an unaccounted dispersion introduces very significant errors in the quantification of DSC-MRI data.

Delay and Dispersion Effects

The combined effects of delay and dispersion were found to introduce large errors in the quantification of DSC data using SVD. The induced error is not simply the addition of the separate errors. For example, a combined delay of 1 sec and a dispersion of $1/\beta$ = 1.5 sec produced a CBF underestimation of ~46% for the gray matter in the adult case. For comparison, the individual underestimation introduced by the delay and the dispersion alone were ~24% and 37%, respectively. It is interesting that for $1/\beta$ larger than ~1.5–2.0 sec, the ratios are not very dependent on the delay value. Therefore, the effect of correcting only for the delay (by shifting back the peak) would reduce only slightly the error in those cases.

In most real situations, delays are likely to have an associated dispersion. Perfusion delays usually occur as a consequence of long arrival delays for the arterial blood to the VOI, for example, as a result of collateral circulation. In these cases, the extra path that the blood must take further spreads the bolus, introducing some dispersion. Therefore, the simulations with delay *and* dispersion are more likely to reflect the situations observed in patients. This has two important consequences. First, a simple shifting of the peak to eliminate the delay is sometimes performed; this will probably only reduce the error but not eliminate it, because there is likely to also be an uncorrected dispersion. Therefore, the results in such cases must still be interpreted cautiously, because the CBF is likely to remain underestimated (see Fig. 6a with delay = 0 sec (filled squares)). Since the error would exaggerate the perfusion deficit, it is not problematic if the CBF map is used mainly to identify abnormal regions. However, it becomes very relevant when regions are defined in terms of flow values, when flow thresholds are determined, or when comparisons between patients or follow-up studies are performed. In all these cases, the conclusions can be erroneous due to the confounding effect of the unaccounted dispersion. Second, there is a problem related to the use of time-to-peak (TTP) maps as a summary parameter (1). These maps will reflect both the delay (time until the arrival of the bolus) and the dispersion (reflected by time from the start of the peak until its maximum). Therefore, they cannot be directly used to identify the regions with delayed perfusion, since a longer TTP could represent, in principle, an area with a dispersed peak but *without* delay. However, as for the previous case the TTP maps are very useful for the identification of abnormal regions because the two effects (delay and dispersion) are additive. For the identification of regions with delayed perfusion, the obvious choice is the use of BAT maps. However, as mentioned above, these maps might be difficult to calculate accurately on a pixel-by-pixel basis due to low SNR.

In summary, the simulations performed in this study have shown that the unaccounted effect of delay and/or dispersion can have a very significant effect in the quantification of DSC data using SVD. When the SNR is large enough, the delay can be corrected by using the information from BAT maps. However, these corrected data can still be inaccurate due to the presence of an uncorrected dispersion. The correction of this dispersion is less straightforward and requires a model for the vasculature (23). Therefore, when no correction for delay

and dispersion is performed, special care must be taken in interpreting the calculated CBF, CBV, and MTT maps if these effects may be present.

ACKNOWLEDGMENT

REFERENCES

1. Calamante F, Thomas DL, Pell GS, Wiersma J, Turner R. Measuring cerebral blood flow using magnetic resonance techniques. J Cereb Blood Flow Metab 1999;19:701–735.
2. Detre JA, Leigh JS, Williams DS, Koretsky AP. Perfusion imaging. Magn Reson Med 1992;23:37–45.
3. Kwong KK, Chesler DA, Weisskoff RM, Donahue KM, Davis TL, Østergaard L, Campbell TA, Rosen BR. MR perfusion studies with T_1-weighted echo-planar imaging. Magn Reson Med 1995;34:878–887.
4. Kim SG. Quantification of relative cerebral blood flow change by flow-sensitive alternating inversion recovery (FAIR) technique. Application to functional mapping. Magn Reson Med 1995;34:293–301.
5. Alsop DC, Detre JA. Reduced transit-time sensitivity in noninvasive magnetic resonance imaging of human cerebral blood-flow. J Cereb Blood Flow Metab 1996;16:1236–1249.
6. Wong EC, Buxton RB, Frank LR. Quantitative imaging of perfusion using a single subtraction (QUIPSS and QUIPSS II). Magn Reson Med 1998;39:702–708.
7. Villringer A, Rosen BR, Belliveau JW, Ackerman JL, Lauffer RB, Buxton RB, Chao YS, Wedeen VJ, Brady TJ. Dynamic imaging with lanthanide chelates in normal brain: contrast due to magnetic-susceptibility effects. Magn Reson Med 1988;6:164–174.
8. Rosen BR, Belliveau JW, Vevea JM, Brady TJ. Perfusion imaging with NMR contrast agents. Magn Reson Med 1990;14:249–265.
9. Østergaard L, Weisskoff RM, Chesler DA, Gyldensted C, Rosen BR. High resolution measurement of cerebral blood flow using intravascular tracer bolus passages. I. Mathematical approach and statistical analysis. Magn Reson Med 1996;36:715–725.
10. Østergaard L, Sorensen AG, Kwong KK, Weisskoff RM, Gyldensted C, Rosen BR. High resolution measurement of cerebral blood flow using intravascular tracer bolus passages. II. Experimental comparison and preliminary results. Magn Reson Med 1996;36:726–736.
11. Liu H-L, Pu Y, Liu Y, Nickerson L, Andrews T, Fox PT, Gao J-H. Cerebral blood flow measurements by dynamic contrast MRI using singular value decomposition with an adaptive threshold. Magn Reson Med 1999;42:167–172.
12. Østergaard L, Johannsen P, Host Poulsen P, Vestergaard Poulsen P, Asboe H, Gee AD, Hansen SB, Cold GE, Gjedde A, Gyldensted C. Cerebral blood flow measurements by magnetic resonance imaging bolus tracking: comparison with [O-15]H2O positron emission tomography in humans. J Cereb Blood Flow Metab 1998;18:935–940.
13. Starmer CF, Clark DO. Computer computations of cardiac output using the gamma function. J Appl Physiol 1970;28:219-220.
14. Boxerman JL, Rosen BR, Weisskoff RM. Signal-to-noise analysis of cerebral blood volume maps from dynamic NMR imaging studies. J Magn Reson Imaging 1997;7:528–537.
15. Vonken EPA, Beekman FJ, Bakker CJG, Viergever MA. Maximum likelihood estimation of cerebral blood flow in dynamic susceptibility contrast MRI. Magn Reson Med 1999;41:343–350.
16. Bassingthwaighte JB, Goresky GA. Volume IV. Microcirculation, part I. Modeling in the analysis of solute and water exchange in the microvasculature. In: Renkin EM, Michel CG, editors. Handbook of physiology section 2: the cardiovascular system. Bethesda: American Physiology Society; 1984. p 549–626.
17. Lassen NA, Henriksen O, Sejrsen P. Volume III. Peripheral circulation, part I. Indicator methods for measurement of organ and tissue blood flow. In: Shepherd JT, Abboud FM, editors. Handbook of physiology section 2: the cardiovascular system. Bethesda: American Physiology Society; 1984. p 21–64.
18. Schreiber WG, Guckel F, Stritzke P, Schmiedek P, Schwartz A, Brix G. Cerebral blood flow and cerebrovascular reserve capacity: estimation by dynamic magnetic resonance imaging. J Cereb Blood Flow Metab 1998;18:1143–1156.
19. Rempp KA, Brix G, Wenz F, Becker CR, Guckel F, Lorenz WJ. Quantification of regional cerebral blood flow and volume with dynamic susceptibility contrast-enhanced MR imaging. Radiology 1994;193:637–641.
20. Koshimoto Y, Yamda H, Kimura H, Maeda M, Tsuchida C, Kawamura Y, Ischii Y. Quantitative analysis of cerebral microvascular hemodynamics with T2-weighted dynamic MR imaging. J Magn Reson Imaging 1999;9:462–467.
21. Armitage P, Berry G. Statistical methods in medical research, 2nd ed. Oxford: Blackwell Scientific; 1987. p 91.
22. Jacquez JA. Partly compartmental and flow systems. In: Compartmental analysis in biology and medicine. Kinetics of distribution of tracer-labeled materials. Amsterdam: Elsevier; 1972. p 84–101.
23. Østergaard L, Chesler DA, Weisskoff RM, Sorensen AG, Rosen BR. Modeling cerebral blood flow and flow heterogeneity from magnetic resonance residue data. J Cereb Blood Flow Metab 1999;19:690–699.